

UNIVERSIDAD SAN FRANCISCO DE QUITO USFQ

Colegio de Ciencias e Ingenierías

**Synthesis of Porous BiFeO₃ Materials and Their Application
in Water Treatment Reactions**

Proyecto de Investigación

Pamela Alejandra Santillán Calderón

Ingeniería Ambiental

Trabajo de titulación de pregrado presentado como requisito
para la obtención del título de Ingeniera Ambiental

Quito, 18 de mayo de 2017

UNIVERSIDAD SAN FRANCISCO DE QUITO USFQ

COLEGIO DE CIENCIAS E INGENIERÍAS

HOJA DE APROBACIÓN DE TRABAJO DE TITULACIÓN

Synthesis of Porous BiFeO₃ Materials and Their Application in Water Treatment Reactions

Pamela Alejandra Santillán Calderón

Calificación:

Thomas Cadenbach, Dr. rer. nat.

Firma del profesor

Quito, 18 de mayo 2018

© Derechos de Autor

Por medio del presente documento certifico que he leído todas las Políticas y Manuales de la Universidad San Francisco de Quito USFQ, incluyendo la Política de Propiedad Intelectual USFQ, y estoy de acuerdo con su contenido, por lo que los derechos de propiedad intelectual del presente trabajo quedan sujetos a lo dispuesto en esas Políticas.

Asimismo, autorizo a la USFQ para que realice la digitalización y publicación de este trabajo en el repositorio virtual, de conformidad a lo dispuesto en el Art. 144 de la Ley Orgánica de Educación Superior.

Firma del estudiante:

Nombre: Pamela Alejandra Santillán Calderón

Código de estudiante: 00116509

C. I.: 1725022626

Lugar, Fecha Quito, 18 mayo de 2018

AGRADECIMIENTOS

A Thomas Cadenbach por brindarme sus conocimientos, guía y paciencia para la realización de mi trabajo de titulación.

A la Universidad de las Fuerzas Armadas ESPE y la Universidad Politécnica Nacional EPN por brindar sus instalaciones, especialistas e instrumentos para la obtención de resultados de SEM, XDR y bandas de energía permitiendo la realización de mí trabajo.

A los profesores y asistentes de laboratorio de Ingeniería Ambiental por su aporte, recomendaciones y apoyo durante la carrera y la realización del trabajo.

A mis padres, a mis hermanos y a mi persona especial por dame el apoyo incondicional y las fuerzas para culminar este trabajo.

Resumen

La industria textil es uno de los sectores más contaminantes debido a la descarga de aguas residuales que presentan colorantes complejos, persistentes y dañinos para la salud y el medio ambiente. La fotocatalisis oxidativa se presenta como alternativa para la degradación de colorantes a partir de la fotocatalisis heterogénea en presencia de luz visible. Se ha escogido el colorante Rhodamine B (RhB) por ser comúnmente utilizado en la industria textil. La remoción del colorante RhB de la fase líquida por fotocatalisis heterogénea se realizó mediante BiFeO₃ (BFO) no dopados y BiFeO₃ dopados. La técnica nanocasting fue utilizada para la síntesis de BFO añadiendo agentes quelantes (ácido cítrico, oxálico y tartárico), mientras que el método de auto combustión fue usado para sintetizar BFO dopados con diferentes contenidos de Gd (Gd_xBi_(1-x)FeO₃, x=0, 0.03, 0.05, 0.10). Los productos obtenidos fueron caracterizados por un Difractor de Rayos-x (XDR), Microscopio de barrido electrónico (SEM) y microscopio de transmisión electrónica (TEM). Los productos obtenidos a partir de nanocasting mostraron fases secundarias y subproductos por lo que dichos materiales no fueron usados para la actividad fotocatalítica. BFO no dopados y dopados en imágenes SEM ilustran redes altamente porosas con rangos de tamaños de poros desde nanómetros hasta micrómetros. También, la medición de la banda de energía pretende tener correlación con la naturaleza porosa de la muestra con rangos de bandas de energía desde 2.22 eV hasta 2.32 eV. Las muestras de Gd dopado- BFO fueron evaluadas por degradación fotocatalítica de RhB en solución acuosa bajo irradiación de luz visible. Comparado con BFO no dopado, muestras Gd dopadas BFO revelan mayor habilidad de absorción y capacidad degradadora. Además, las condiciones óptimas relacionadas a una degradación de RhB (77%) fueron alcanzadas con 5 mg/L de solución RhB a un pH 4, Gd dopado 5%-BFO y la aplicación de 100 mg de fotocatalizador. Estos resultados revelan la importancia de identificar la técnica óptima para sintetizar el fotocatalizador, así como los parámetros óptimos para el proceso de degradación con el fin de mejorar la tasa y eficiencia de degradación.

Palabras Claves: Colorantes, Rhodamine B, Bismuto férrico, BiFeO₃, Fotocatalisis, Semiconductor, Auto-Combustión, Nanocasting, SBA-15, Glicina

Abstract

Textile industry is one of the major contaminant sector due to wastewater discharge with complex, persistent and harmful dyes. Photocatalysis oxidation process tend to be an attractive mechanism for dye degradation based in heterogeneous photocatalysis under visible light irradiation. Rhodamine B dye (RhB) was chosen because is a commonly usage dye in textile industry. Heterogeneous photocatalytic removal of Rhodamine B (RhB) dye from liquid phase was performed using undoped BiFeO₃ (BFO) and Gd doped BiFeO₃ photocatalysts. Nanocasting technique was used for undoped BFO synthesis by adding chelating reagents (citric, oxalic and tartaric acid), while autocombustion method was used for Gd doped BFO materials at different Gd doping contents (Gd_xBi_(1-x)FeO₃, x=0, 0.03, 0.05, 0.10). The obtain products were characterized by X-ray diffraction, scanning electron microscopy, transmission electron microscopy. Nanocasting products showed secondary phases and byproducts in XRD, consequently materials was not used for photocatalytic activity. Undoped and Gd doped BFO materials in SEM images illustrated highly porous network and irregular pore size ranges from nanometers to micrometers. Also, band gap measurements seem to be correlated to the porous nature of the sample with band gaps range from 2.22 eV to 2.32 eV. Gd doped BFO samples were evaluated by photocatalytic degradation of RhB in aqueous solution under visible light irradiation. It was found that increasing Gd doping, significantly affect the photocatalytic activity. Compared to pure BFO, the Gd doped BFO samples reveled enhance absorption as well as degradation capacity. Moreover, the optimum conditions for the highest RhB degradation (77%) was achieved for a 5 mg/L RhB solution at pH 4, a doped Gd5%-BFO and a loading of 100 mg. These results clearly reveal the importance of identifying the optimum technique for the photocatalyst synthesis, as well as optimum parameters for the degradation process in order to enhance the rate and degradation efficiency.

Keywords: Dyes, Rhodamine B, bismuth ferrite, BiFeO₃, Photocatalysis, Semiconductor, Auto-Combustion, Nanocasting, SBA-15, Glycine

Content

Resumen	5
Abstract	6
1. Introduction.....	10
2. Experimental Section.....	16
2.1. Synthesis of BiFeO ₃ Nanoparticles by Nanocasting.....	16
2.2. Synthesis of BiFeO ₃ Nanoparticles by Autocombustion	18
2.3. Characterization.....	21
2.4. Evaluation of Photocatalytic Activity.....	22
3. Results and Discussion	27
3.1. Materials Characterization.....	27
3.1.1. Nanocasting Technique	27
3.1.2. Autocombustion Technique.....	29
3.2. Band gap measurements	32
3.3. Photocatalytic Activity.....	34
3.4. Optimizing Photocatalysis	37
3.4.1. Effect of Catalyst Concentration	37
3.4.2. Influence of Initial pH on photodegradation process.....	37
4. Conclusions.....	38
5. References	41
6. Annexes	45

List of Figures

Figure 1: Scheme of photocatalysis using a semiconductor.....	12
Figure 2: Nanocasting principle for mesoporous materials and BiFeO ₃ replicas (right) using SBA-15 (left).....	14
Figure 3: Molecular structure of Rhodamine B.	22
Figure 4: Calibration curve for Rhodamine B.....	23
Figure 5: Experimental setup of the photocatalytic process.....	24
Figure 6: Spectral wavelength of the photoreactor.	24
Figure 7: Vis Absorption spectra of Gd5% BFO sample.	26
Figure 8: TEM images of BFO nanoparticles sample by hard template technique.	27
Figure 9: XRD patterns of BFO using oxalic acid in nanocasting technique.	29
Figure 10 : (a) XRD patterns of Bi _{1-x} Gd _x FeO ₃ (x=0.00, 0.03, 0.05, and 0.10); (b) the zoom-in patterns of Bi _{1-x} Gd _x FeO ₃ in the range of 30° to 34°.....	30
Figure 11: SEM images of synthesized samples: (a) pure BFO; (b) Gd 3%-BFO, (c) Gd 5%-BFO, (d) Gd 10%-BFO. The scale bar to all images is of 10 μm.....	32
Figure 12: Band gaps plots: (a) pure BFO; (b) Gd 3%-BFO, (c) Gd 5%-BFO, (d) Gd 10%-BFO.....	33
Figure 13: Photocatalytic degradation of RhB as a function of irradiation time (min) under visible light catalyzed by pure BFO, Gd doped BFO samples, dark and blank controls.	35
Figure 14: Pseudo- first order kinetics reaction fitting data for the photocatalytic degradation of RhB.....	36
Figure 15: Catalyst Concentration and pH effect on photocatalytic efficiency using Gd5% doped BFO sample.....	38
Figure 16: Constructed photo reactor for photocatalytic degradation of RhB, by Thomas Cadenbach	45

List of Tables

Table 1: Advantages and Disadvantages of dye removal common methods from industrial effluents.....	11
Table 2: Calcination temperatures, time and rates for BFO synthesis.	18
Table 3: Reagents quantities for pure BFO and Gd doped BFO synthesis.	20
Table 4: Pseudo first order rate constants for RhB photodegradation and linear regression coefficients of each BFO samples.....	36

1. Introduction

Water plays an important role in natural ecosystems as an essential element for sustenance and biological processes on the planet Earth (Paredes, 2013). Over 75% of the Earth surface is covered with water, of which only 2.5% correspond to fresh water and less than 1% of the world freshwater is accessible for direct human uses (Rinkesh, 2009). Nowadays, freshwater systems such as rivers, lakes, wetlands and aquifers are drying up or being polluted due to anthropogenic activities (Water Scarcity, 2017). In addition, many water systems that maintain functional ecosystem services feed an increasingly human population and consequently have become stressed.

One of the major water pollution contributors is the textile industry. As a fact, 100 liters of wastewater are produced for every kilogram of textile product which is equivalent to 3.7 million liters per day worldwide (Kant, 2012). According to The World Bank, 17 to 20% of industrial water pollution is attributed to textile dyeing treatment. The presence of dyes even at very low concentrations in effluents is highly visible and undesirable (Nigam, Armour, Banat, Singh, & Marchant, 2000). Amongst the many different variations of dyes water-soluble dyes are the most problematic (Willmott, Guthrie, & Nelson, 1998) because of their capacity to bond with colloidal matter and their interferences with the oxygen solubility and self-purification process of water (Kant, 2012). Due to their complex chemical structure, dyes are resistant to degradation by exposure of light, water and many chemicals (Poots, V & McKay, 1976). Thus, dyes often cause problems to aquatic ecosystems and serious health-risk due to their stability and toxicity.

For instance, protection and preservation of the environment as well as water system quality and human health have been the key motivation to develop methods for dye removal from water such as biodegradation, adsorption, coagulation, biodegradation and advanced oxidation processes (Khataee & Kasiri, 2010). Advantages and

disadvantages of these methods are summarized in Table 1. During the last decade, advanced oxidation processes (AOP) has been attractive as an alternative path for dyes removal. Heterogeneous catalysis had shown to be successful for degradation of hazardous compounds (Mamun, Kurny, & Gulshan, 2017).

Table 1: Advantages and Disadvantages of dye removal common methods from industrial effluents.

Physical/chemical methods	Advantages	Disadvantages
Ozonation	No alteration of volume	Short half-life (20 min)
Electrochemical	No sludge production	Formation of by-products
Activated Carbon	Removal of varieties of dyes	Very expensive
Membrane Filtration	Remove all types of dyes	Side reactions prevent commercial application
Ion Exchange	Regeneration: no adsorbent loss	Not effective for all dyes
Coagulation	Economically feasible	High sludge production
Electron beam irradiation under pressurized oxygen	Effective oxidation at lab scale	Uses big amount of dissolved O ₂
Anaerobic bioremediation	Biogas production	Only Azo reduction

Source: (Robinson, McMullan, Marchant, & Nigam, 2001)

The use of a heterogeneous photocatalyst is extensively investigated due to the advantage of the usually completed mineralization of organic pollutants to CO₂ and H₂O taking place at room temperature (Mamun, Kurny, & Gulshan, 2017). As described in Figure 2, photons coming from an energy source such as sunlight, irradiate the photocatalyst surface. If the energy of the irradiating source is high enough, electrons situated in the valence band (VB) of the photocatalyst, are excited to the conduction band (CB), generating electron holes, Eq. (1) (note, the energy gap between valence and conductive band is called band gap). Those electrons holes can react with H₂O to

form oxidizing hydroxyl radicals (OH^*) Eq. (2). Subsequently, these strongly oxidizing radicals react with dyes (organic pollutant) to CO_2 and H_2O , Eq. (3). Additional reactions could take place such as the recombination of electrons and holes to produce thermal energy, Eq. (4) which is an undesirable reaction because it is limiting the photocatalytic activity (Schneider, et al., 2014). The excited electrons can also react with O_2 to generate superoxide anions ($\text{O}_2^{\bullet -}$), Eq. (5) (Mamun, Kurny, & Gulshan, 2017).

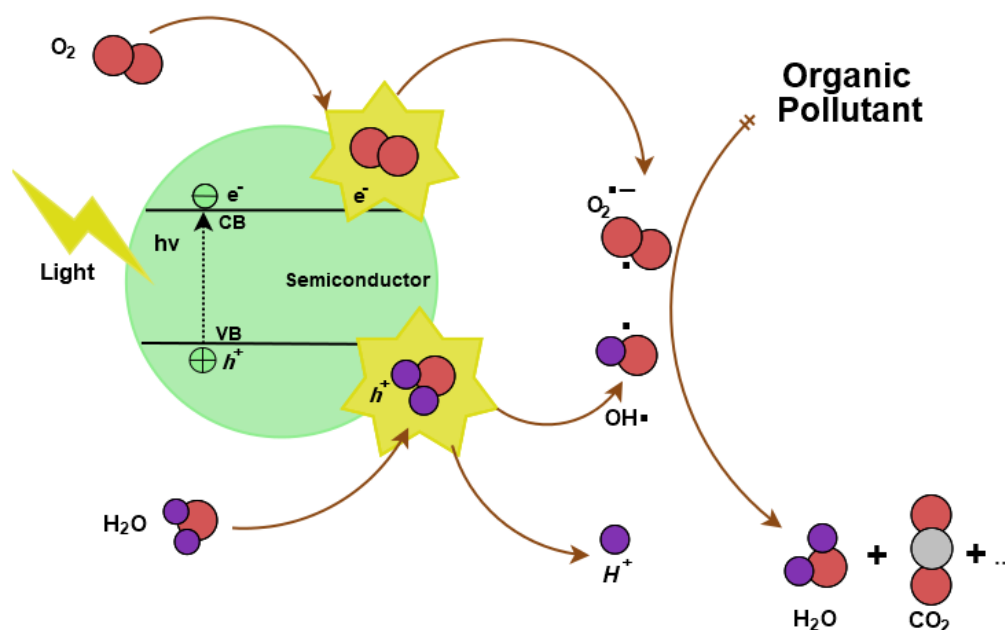


Figure 1: Scheme of photocatalysis using a semiconductor.

In general, photogeneration of radical species in catalyst/UV-Vis can be summarized as follows (Kormann, Bahnemann, & Hoffman, 1988):



There are major investigations involving TiO_2 as a photocatalyst because it is easy to produce, cheap, photo sensible and stable (Hashimoto, Irie, & Fujishima, 2005). However, TiO_2 has a high band gap (3.2 eV) so it needs light in the ultraviolet energy range to be activated. Considering the UV light energy constitute 2% of the total solar energy, expensive equipment is needed when using TiO_2 (Dao, et al., 2016). Thus, designing new photocatalysts with lower bandgaps, high stability, major generation and recovery capacity represent an attractive solution in the field of wastewater treatment.

Recently, researchers have shown interest in the application of high performance lead-free ferroelectric and magnetoelectric materials. At room temperature, those properties are found in bismuth ferrite (BiFeO_3), abbreviated for the research as BFO, a semiconductor with high chemical stability, an intrinsic electric polarization field and a narrow energy bandgap (~ 2.2 eV). In contrast to traditional catalysts such as ZnO , Al_2O_3 , FeO_3 y TiO_2 (Papadas, Kota, Kanatzidis, & Armatas, 2012), bismuth ferrite uses visible light to mineralize organic pollutants. This is mainly important because visible light energy occupies about 48% of the total solar energy (Gao, et al., 2014).

Therefore, developing bismuth ferrite can be a promising photocatalyst for organic pollutants degradation. In recent years, various techniques such as sol-gel method, hydrothermal, co-precipitation, autocombustion, and others methods have been employed to synthesized BFO particles. Since, BFO photocatalysis is a heterogeneous catalytic process and reactivity depends largely on surface area, synthesizing porous materials is one of the approaches to obtain a highly reactive catalyst. Thus, two different techniques for obtaining porous materials were used, i.e. nanocasting and autocombustion.

The first one is a nanocasting technique using a hard template in a wet impregnation-calcination method. This technique could be compared as sand castle building, where the sand is an analogy of the precursors used to form the photocatalyst material and the castle template is related to the silica template used to obtain a desirable structure.

Usually, an excess amount of solvent is often used to form a homogeneous solution. During the evaporation of the solvent, the precursors (hydrated bismuth nitrate and hydrated iron nitrate) are expected to migrate into the pore systems of a silica template due to capillary forces. After calcination, the pore volume which was occupied by the precursors will shrink intensely. This reduction provides further space for additional impregnations. Due to the structure giving template a continuous and ordered structure is obtained. In addition, in order to generate high-quality ordered porous metal oxides through this nanocasting method, it is necessary to perform multiple impregnations steps (Deng, Chen, & Tüysüz, 2016). For our research, 2 impregnations were applied. In the first impregnation synthesis, the silica template is filled with an adequate amount of precursors. Then, calcination at lower temperatures forms the desired oxide and provides area for the next impregnation. After a second impregnation, final calcination at higher temperatures results in the oxide/silica composite, Figure 2. Highly ordered porous materials can be obtained by removing the silica template.

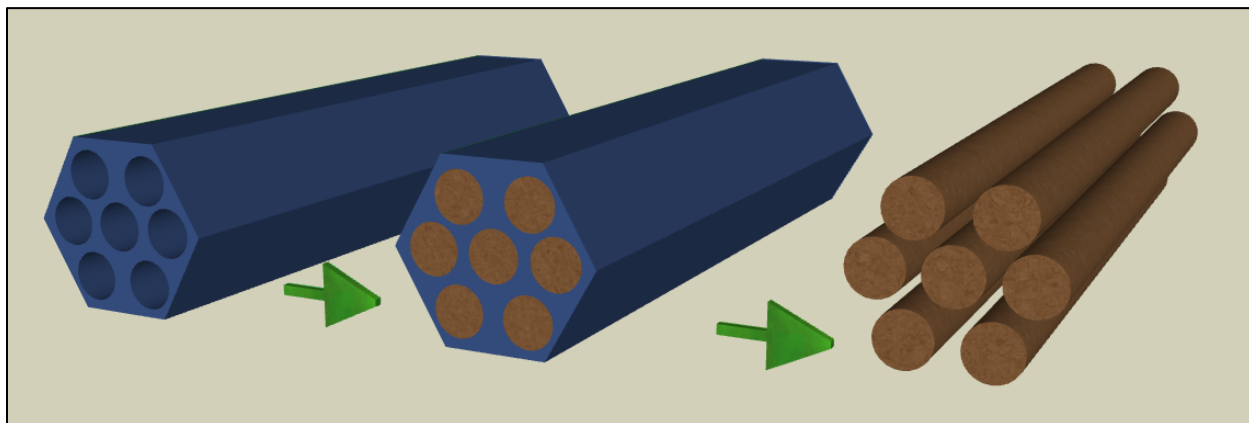


Figure 2: Nanocasting principle for mesoporous materials and BiFeO_3 replicas (right) using SBA-15 (left).

The second synthesizing technique is autocombustion. The simplicity, energy-saving route uses certain concentration levels of BiNO_3 and FeNO_3 as precursor materials (Kumar, 2009), a glycine/nitric acid mixture as fuel and distilled water to obtain a

homogenous mixture. The mixture is then heated up in order to evaporate solvents. A gel is formed until the ignition temperature of the mixture is reached which then leads to a spontaneous self-sustaining combustion reaction. The redox system produces a strongly exothermic reaction with temperatures inside the flame of $\sim 1285^{\circ}\text{C}$, providing the energy for the formation of BiFeO_3 porous material. The main advantage of the autocombustion method is the high purity, desired size and shape of the material due to the high temperatures involved. In addition, the fast release of large amounts of combustion gases CO_2 , H_2O , NO , NO_2 , NH_3 during the reaction creates a porous network with a wide pore size distribution (Kumar, 2009), (Hwang, Sheng, & Huang, 2005)

The application of BiFeO_3 (BFO) during a photocatalysis process could form byproducts (Ortiz, et al., 2013) and amorphous phases could alter the electron/hole recombination kinetics, disturbing the photocatalytic efficiency of BiFeO_3 (Ortiz, et al., 2013). Also, remaining NO_3^- and other anions could be adsorbed onto the catalyst surface, hence surface reactivity will change. For that reason, within the autocombustion method, a different atom (Gd) was used as a dopant in the bismuth ferrite photocatalyst synthesis in order to obtain high purity BiFeO_3 and to improve photocatalytic activity. Rare earth dopants within the lattice of the photocatalyst could act as electron trapping spots in order to improve the production and separation of photogenerated electron-hole pairs during the process of photocatalytic reaction (Zhang, et al., 2016).

There is a huge effort to understand the influence of Gd-doped BFO in photocatalysis and to relate the physical properties of the synthesized catalyst with the photocatalytic efficiency. Therefore, the main objective of this research project is to focus on photocatalytic degradation performance of BiFeO_3 catalysts synthesized by a nanocasting technique using SBA-15 as a hard template and by an auto combustion technique using a glycine/ HNO_3 mixture as the combustion fuel. The samples were characterized by X-ray diffraction (XRD), Scanning electron microscopy (SEM), transmission electron microscopy (TEM) and band gap measurements. The dye used in these studies is one of the most used dye in textile industry, Rhodamine-B. Our aim, is

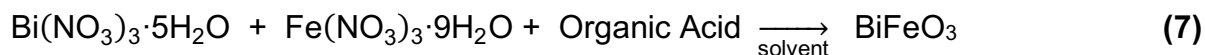
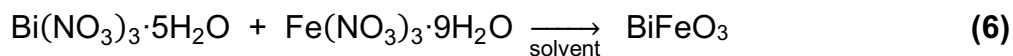
to evaluate the activity of photocatalytic process of the synthesized BiFeO₃ samples by examining the degradation of Rhodamine-B under solar irradiation in a laboratory scale.

2. Experimental Section

2.1. Synthesis of BiFeO₃ Nanoparticles by Nanocasting

The reagents used in the synthesis were bismuth nitrate pentahydrate (Bi(NO₃)₃·5H₂O), iron nitrate nonahydrate (Fe(NO₃)₃·9H₂O), 99% ethanol(CH₃CH₂OH), concentrated nitric acid (HNO₃), citric acid (C₆H₈O₇), oxalic acid (HOOC-COOH), tartaric acid (C₄H₆O₆), distilled water and SBA-15.

In order to study the effect of organic acids in the preparation of BFO using a hard-templating technique, several organic acids were employed in the synthesis, such as oxalic acid (HOOC-COOH), citric acid (C₆H₈O₇) and tartaric acid(C₄H₆O₆). General reaction equations are described as following:



*Organic Acid= citric, oxalic and tartaric acid

Reaction 1

3 mmol each of Bi(NO₃)₃·5H₂O and Fe(NO₃)₃·9H₂O, previously grinded, were dissolved in a 10 mL of ethanol. In order to obtain an equimolar solution, 2 mL of conc. HNO₃ and 10 mL of H₂O were added (Nair, Kaliaguine, & Kleitz, 2014). The homogeneous solution was then added slowly to 1g of SBA-15. The mixture was stirred for 4h at room temperature. Subsequently, solvents were evaporated in an oven at 65°C

for 48h. The obtain sample was grounded well in a mortar, drying and calcination was performed as shown in Table 2.

Reaction 2

3 mmol each of $\text{Bi}(\text{NO}_3)_3 \cdot 5\text{H}_2\text{O}$ and $\text{Fe}(\text{NO}_3)_3 \cdot 9\text{H}_2\text{O}$, previously grinded, were dissolved in a 10 mL of ethanol containing 3 mmol of citric acid. In addition, 4 mL of conc. HNO_3 and 10 mL of H_2O were added to the mixture. The homogeneous solution was then added slowly to 1g of SBA-15. The mixture was stirred for 4h at room temperature. Subsequently, solvents were evaporated in an oven at 65°C for 48h. The obtain sample was grounded well in a mortar, drying and calcination was performed as shown in Table 2.

Reaction 3

3 mmol each of $\text{Bi}(\text{NO}_3)_3 \cdot 5\text{H}_2\text{O}$ and $\text{Fe}(\text{NO}_3)_3 \cdot 9\text{H}_2\text{O}$, previously grinded, were dissolved in a 10 mL of ethanol containing 3 mmol of oxalic acid, 3 mL of conc. HNO_3 and 10 mL of H_2O were added to the mixture. The homogeneous solution was then added slowly to 1g of SBA-15. The mixture was stirred for 4h at room temperature. Subsequently, solvents were evaporated in an oven at 65°C for 48h. The obtain sample was grounded well in a mortar, drying and calcination was performed as shown in Table 2.

Reaction 4 – Attempted synthesis of BFO using tartaric acid

3 mmol each of $\text{Bi}(\text{NO}_3)_3 \cdot 5\text{H}_2\text{O}$ and $\text{Fe}(\text{NO}_3)_3 \cdot 9\text{H}_2\text{O}$, previously grinded, were dissolved in a 10 mL of ethanol containing 3 mmol of tartaric acid, 10 mL of conc. HNO_3 and 10 mL of H_2O were added to the mixture. The homogeneous solution was then added slowly to 1g of SBA-15. The mixture was stirred for 4h at room temperature. However, an undesirable spontaneous exothermic reaction occurred during the stirring. The reason was the equimolar presence of nitric acid and ethanol, resulting in the spontaneous decomposition of HNO_3 and the production of nitrogen oxides gases being visible as a violent and toxic fume (Dhananjai, 2016). The synthesis technique using tartaric acid as an organic acid was no longer performed.

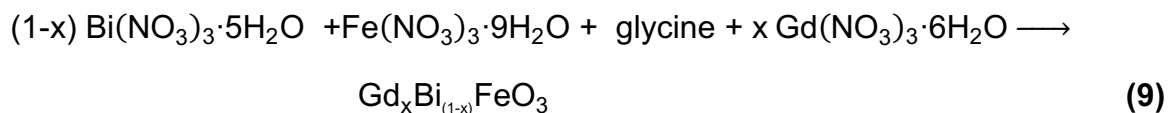
Table 2: Calcination temperatures, time and rates for BFO synthesis.

Phases	Reaction 1	Reaction 2	Reaction 3
Heat rate 1 (°C/min)	1	1	1
Drying Temperature 1 (°C)	200	200	200
Drying Time 1 (h)	4	4	4
Calcination rate 1 (°C/min)	2	2	2
Calcination Temperature 1 (°C)	500	500	500
Calcination Time 1 (h)	4	4	4
Heat rate 2 (°C/min)	1	1	1
Drying Temperature 2 (°C)	200	200	200
Drying Time 2 (h)	4	4	4
Final Calcination rate (°C/min)	2	2	2
Final Calcination Temperature (°C)	500	500	500
Final Calcination Time (h)	6	4	4

2.2. Synthesis of BiFeO₃ Nanoparticles by Autocombustion

The reagents used in the synthesis were bismuth nitrate pentahydrate (Bi(NO₃)₃·5H₂O), iron nitrate nonahydrate (Fe(NO₃)₃·9H₂O), conc. Nitric acid (HNO₃), distilled water, 99% glycine(H₂NCH₂COOH) as an organic species used to complex Bi³⁺ and Fe³⁺ cations in aqueous solution (Ortiz, et al., 2013); gadolinium nitrate hexahydrate (Gd(NO₃)₃·6H₂O) and distilled water. Four samples were synthesized, each one with different concentrations of Gd(NO₃)₃·6H₂O. A 100mL beaker was used for each reaction. Table 3, summarized reagents quantities for each reaction. General reaction equations are described as following:





$$*x = 0.03, 0.05, 0.10$$

Reaction 5 – Synthesis of BiFeO₃:

4 mmol of Bi(NO₃)₃·5H₂O, 4 mmol of Fe(NO₃)₃·9H₂O and 8 mmol of glycine were dissolved in a mixture of 40 mL of distilled water and 2.8mL of conc. HNO₃ (Ortiz, et al., 2013) and stirred at room temperature. Then, the mixture was heated while stirring at 600 rpm, in order to evaporate all solvents. Once all solvents were evaporated a combustion reaction took place. In each reaction, the organic species acted as the reducing agent while NO₃⁻ was the oxidizing agent (Ortiz, et al., 2013). The brown powder obtained was heated to 125°C in the oven for 1h in order to assure that all solvents were evaporated. Then, all samples were calcinated at 350°C for 1h and then 500°C for 1h at a heat rate of 3 °C/min.

Reaction 6 – Synthesis of Bi_{0.97}Gd_{0.03}FeO₃

3.88 mmol of Bi(NO₃)₃·5H₂O, 4 mmol of Fe(NO₃)₃·9H₂O, plus 0.12 mmol Gd(NO₃)₃·6H₂O, and 8 mmol of glycine were dissolved in a mixture and subsequently stirred at room temperature. Then the mixture was heated while stirring at 600 rpm, in order to evaporate all solvents. Once all solvents were evaporated a combustion reaction took place. In each reaction, the organic species acted as the reducing agent while NO₃⁻ was the oxidizing agent (Ortiz, et al., 2013). The brown powder obtained was heated to 125°C in the oven for 1h in order to assure that all solvents were evaporated. Then, all samples were calcinated at 350°C for 1h and then 500°C for 1h at a heat rate of 3 °C/min.

Reaction 7 – Synthesis of Bi_{0.95}Gd_{0.05}FeO₃

For the second reaction, 3.8 mmol of $\text{Bi}(\text{NO}_3)_3 \cdot 5\text{H}_2\text{O}$, plus 0.2 mmol $\text{Gd}(\text{NO}_3)_3 \cdot 6\text{H}_2\text{O}$, 4 mmol of $\text{Fe}(\text{NO}_3)_3 \cdot 9\text{H}_2\text{O}$ and 8 mmol of glycine were dissolved in a mixture of 40 mL of distilled water and 2.8 mL of conc. HNO_3 and subsequently stirred at room temperature. Then, the mixture was heated while stirring at 600 rpm, in order to evaporate all solvents. Once all solvents were evaporated a combustion reaction took place. In each reaction, the organic species acted as the reducing agent while NO_3^- was the oxidizing agent (Ortiz, et al., 2013). The brown powder obtained was heated to 125°C in the oven for 1h in order to assure that all solvents were evaporated. Then, all samples were calcinated at 350°C for 1h and then 500°C for 1h at a heat rate of $3^\circ\text{C}/\text{min}$.

Reaction 8 – Synthesis of $\text{Bi}_{0.90}\text{Gd}_{0.10}\text{FeO}_3$

3.6 mmol of $\text{Bi}(\text{NO}_3)_3 \cdot 5\text{H}_2\text{O}$, 4 mmol of $\text{Fe}(\text{NO}_3)_3 \cdot 9\text{H}_2\text{O}$, plus 0.4 mmol $\text{Gd}(\text{NO}_3)_3 \cdot 6\text{H}_2\text{O}$, and 8 mmol of glycine were dissolved in a mixture, subsequently stirred at room temperature, of 40 mL of distilled water and 2.8 mL of 1M HNO_3 . Then, the mixture was heated while stirring at 600 rpm, in order to evaporate all solvents. Once all solvent was evaporated a combustion reaction took place. In each reaction, the organic species acted as the reducing agent while NO_3^- was the oxidizing agent (Ortiz, et al., 2013). The brown powder obtained was heated to 125°C in the oven for 1h in order to assure that all solvents was evaporated. Then, all samples were calcinated at 350°C for 1h and then 500°C for 1h at a heat rate of $3^\circ\text{C}/\text{min}$.

Table 3: Reagents quantities for pure BFO and Gd doped BFO synthesis.

Reagents	Units	Reaction 5	Reaction 6	Reaction 7	Reaction 8
$\text{Bi}(\text{NO}_3)_3 \cdot 5\text{H}_2\text{O}$	mmol	4	3.88	3.8	3.6
	g	1.9403	1.8821	1.8433	1.7463
$\text{Fe}(\text{NO}_3)_3 \cdot 9\text{H}_2\text{O}$	mmol	4	4	4	4
	g	1.616	1.616	1.616	1.616
$\text{Gd}(\text{NO}_3)_3 \cdot 6\text{H}_2\text{O}$	mmol	0	0.12	0.2	0.4

	g	0	0.0542	0.0903	0.1805
Glycine	mmol	8	8	8	8
	g	0.6006	0.6006	0.6006	0.6006
H ₂ O	ml	40	40	40	40
HNO ₃	ml	2.8	2.8	2.8	2.8

2.3. Characterization

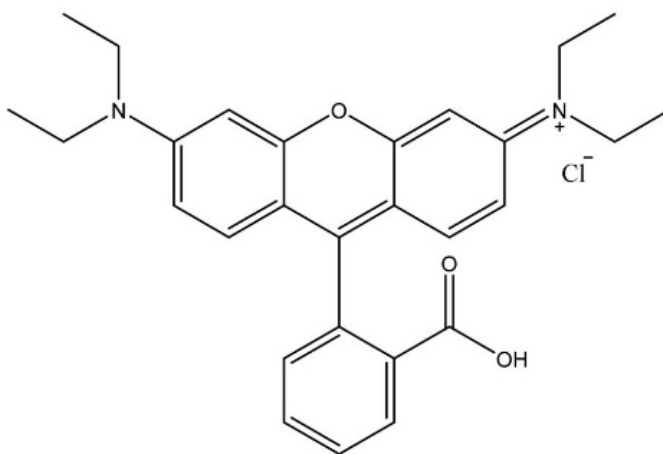
The synthesized materials were structurally characterized with a PANalytical EMPYREAN diffractometer with a 2 θ configuration (generator-detector) equipped with a Cu-tube ($\lambda=1.54$ Å) and a XCELERATOR detector. Particle size and morphology of the samples obtained by autocombustion were analyzed by scanning electron microscopy (SEM) using a VEGA 3 TESCAN microscope. The particle size and morphology of the samples obtained by the nanocasting technique were evaluated using a transmission electron microscopy (TEM), FEI Tecnai G2 spirit twin.

Diffuse reflectance measurements were made with a system (Ocean Optics, Dunedin, FL) consisting of a UV-Vis-NIR lamp to illuminate the surface of the flattened powder samples (200-960 nm), a diffuse reflectance probe set as 6 illumination fibers around 1 read fiber which faces the sample surface at a 45° angle. Both the reference (Teflon standard) and the reflection spectra were acquired with a HR4000CG spectrometer for given integration times. Spectra were suitably transformed to be analyzed with the Kubelka-Munk model in order to obtain the band gap value (Kubelka & Munk, 1931).

Photocatalytic degradation were measured with a GENESYS 30™ spectrophotometer with a Tungsten-Halogen light source, a 5.0 nm spectral bandwidth, and silicon photodiode detector. The spectra fittings were made with the Thermo Scientific™ VISIONlite PC software.

2.4. Evaluation of Photocatalytic Activity

Photocatalytic activities of the samples were evaluated by the photocatalytic degradation of Rhodamine B (RhB) under visible light. Rhodamine B, structure shown in Figure 3, was chosen for this research project because it is commonly used as a synthetic soluble dye in textile industry. Furthermore, the interpretation of its UV-VIS spectrum is rather easy due to an isolated band at 555 nm. In addition, the environmental relevance of RhB is given due its persistent, corrosive, harmful, highly toxic and carcinogenic nature (National Center for Biotechnology Information, s.f.). The international Agency of Research on Cancer (IARC) classified rhodamine B in group 3 which is not classifiable as to its carcinogenicity to humans. Although, it was carcinogenic in rats when injected subcutaneously, producing local sarcomas (IARC, 1998).



Source: (National Center for Biotechnology Information, s.f.)

Figure 3: Molecular structure of Rhodamine B.

A Rhodamine B VIS absorbance standard curve was generated by dissolving 5mg Rhodamine B in 1L of water. This solution was then diluted to different concentrations in distilled water. Then the absorbance of 6 diluted solutions were measured in the spectrophotometer from 400 nm to 1000 nm. It should be noted, that the intensity of the

absorption peak of RhB (around 554 nm) is directly proportional to the molecule concentration which is described by the Beer-Lambert equation (Bai, et al., 2016).

$$A = \log_{10} \frac{I_0}{I} = \epsilon l c \quad (10)$$

where, A is the absorption of light by the sample, I is the light intensity once it passes through the sample, I_0 is the initial light intensity, ϵ is the wavelength molar absorptivity coefficient ($M^{-1}cm^{-1}$), b is the path length (cm) and c de sample concentration (M).

Figure 4, represent calibration curve based on the Beer-Lambert law, equation (10) in order to quantify RhB concentration during photocatalytic activity.

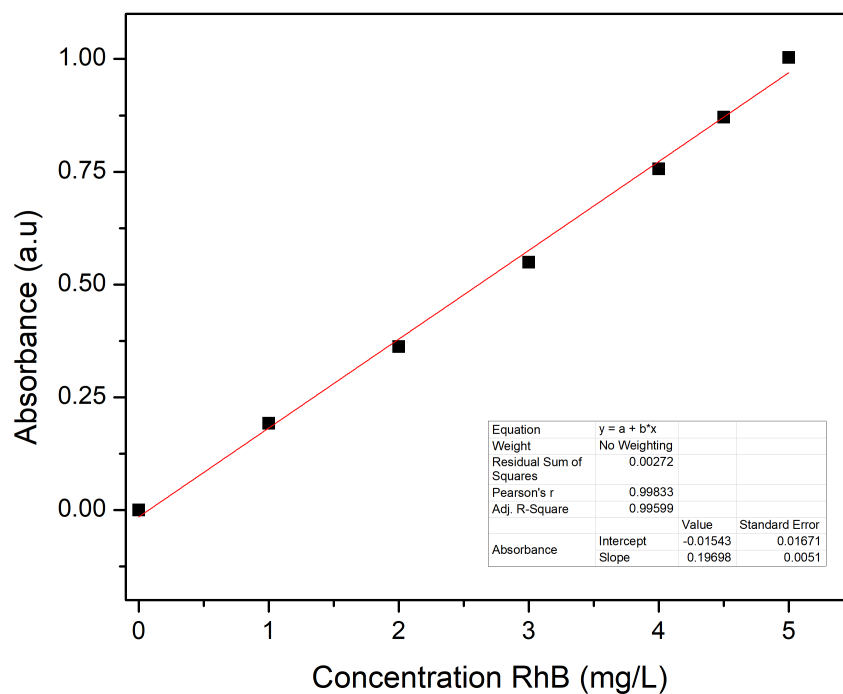


Figure 4: Calibration curve for Rhodamine B.

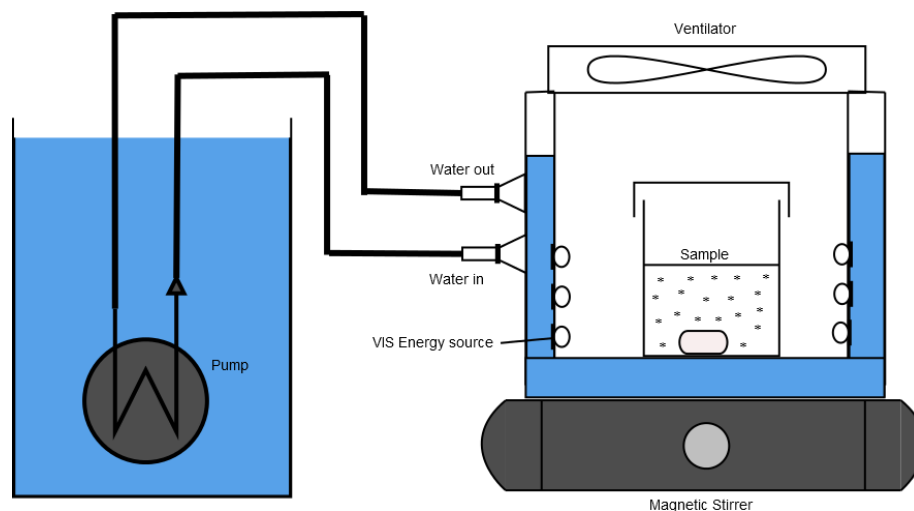


Figure 5: Experimental setup of the photocatalytic process.

A self-constructed air- and water-cooled photoreactor equipped with high intensity LEDs with a spectral wavelength of 400-700nm, as shown in Figure 5. For the project, continuous visible light is necessary as a sunlight simulator, high intensity LEDs, located around the photoreactor walls; provided a spectral wavelength of 400-700 nm, as described in figure 6.

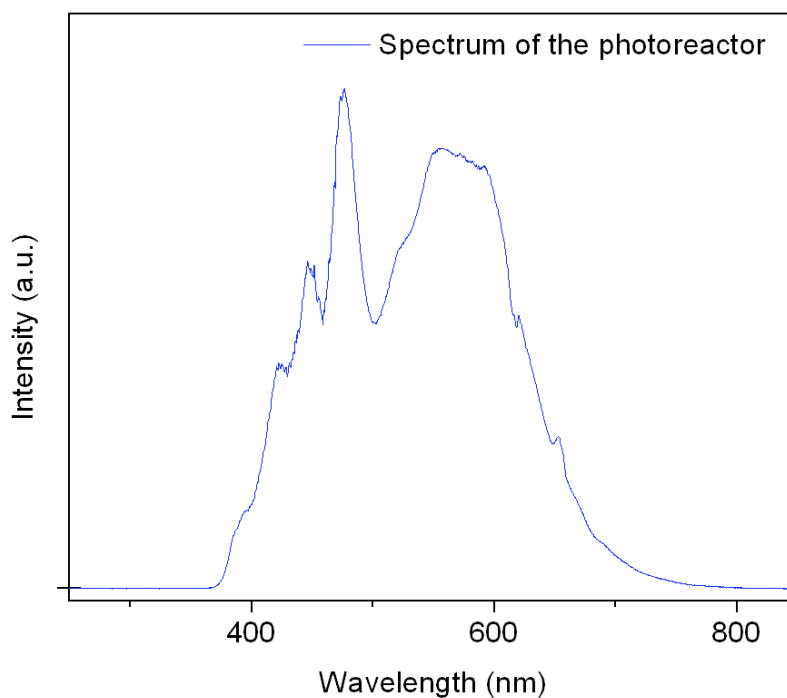


Figure 6: Spectral wavelength of the photoreactor.

In a typical experiment, degradation trials were carried out in a 100 mL beaker equipped with magnetic stirring bar. 50 mg BFO particles were dispersed into 50 mL of 5mg/L RhB aqueous solution. The heterogeneous mixture was magnetically stirred in dark for 1h to achieve an adsorption-desorption equilibrium between the photocatalyst and the dye. The RhB concentration after the establishment of an equilibrium was determined by measuring the absorbance of light at 554 nm.

Afterwards, temperature was monitored and kept constant at room temperature during the photocatalytic process due to ventilation and cold water circulation. Every 30 minutes for 4h, a small quantity (2.5 mL) of the solution was taken and centrifuged at 6 000 rpm for 1 min to separate the catalyst powder from the solution. Then, the maximum intensity of the main absorption peak of RhB was measured using the GENESYS 30™ spectrophotometer.

Essentially, for each sample, a final RhB concentration and corresponding photodegradation efficiency was determined using the RhB standard curve and the maximum absorption peak. In addition, the kinetics of the photocatalytic degradation of diluted RhB solution with BFO under visible irradiation had been modeled by Langmuir-Hinshelwood equation. Diluted RhB solution followed a pseudo first order reaction. For that instance, the reaction rate constant can be directly obtained using the following equation:

$$\ln \frac{C}{C_0} = -k t \quad (11)$$

Here, C_0 and C corresponds to the concentrations of RhB at different irradiation time of t_0 and t , respectively, whereas k is the pseudo-first-order rate constant of photocatalytic process (min^{-1}).

Finally, optimized degradation conditions using the photocatalyst with higher degradation efficiency were evaluated in new experiments at a lower pH and varying catalyst: dye ratio.

To evaluate the decrease of concentration of RhB by photodegradation and influence of Gd doping on the optical absorption of BFO, UV-Vis spectra of BFO samples were measured at room temperature, as represent in Figure 7.

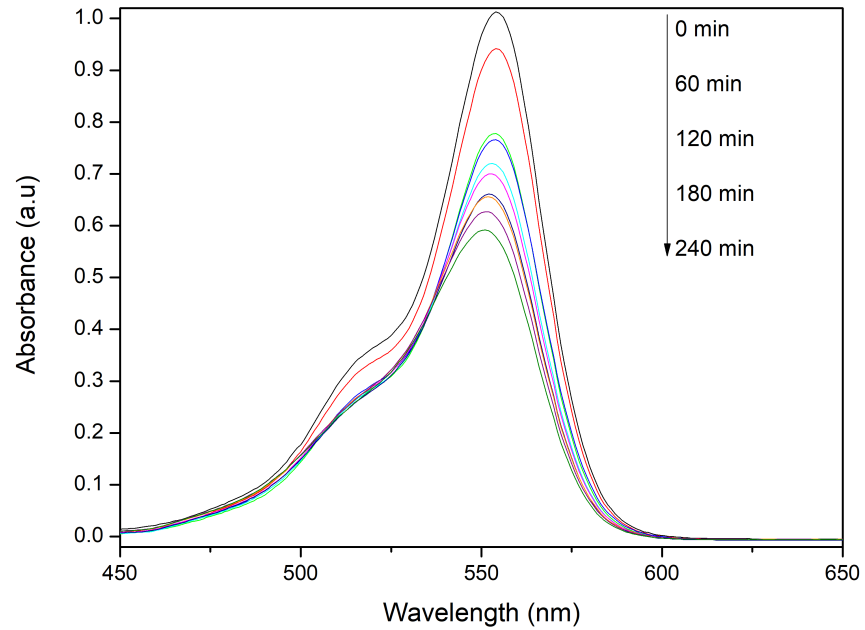


Figure 7: Vis Absorption spectra of Gd5% BFO sample.

3. Results and Discussion

3.1. Materials Characterization

3.1.1. Nanocasting Technique

TEM images of BFO samples using the hard template technique are displayed in Figure 8. As shown in these images the samples are highly agglomerated nanoparticles with diameter of 8nm.

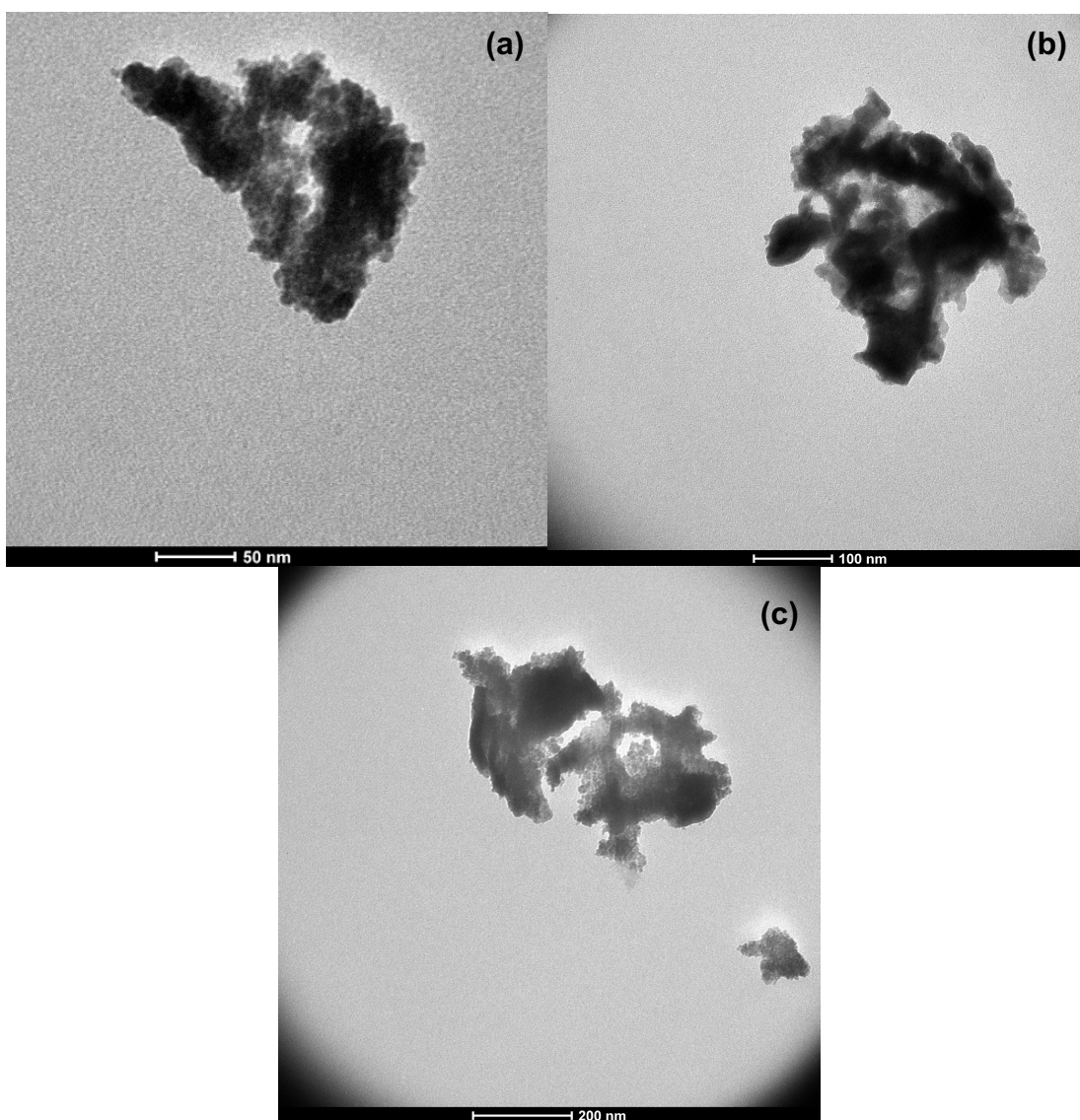


Figure 8: TEM images of BFO nanoparticles sample by hard template technique.

These images suggest that the impregnation of SBA-15 by the metal precursors was successful, i.e. the particle formation occurred in the channel of SBA-15 as anticipated. However, X-ray diffraction results were not as expected. Figure 9, represents the sample obtained by the nanocasting technique and using oxalic acid as a chelating reagent.

XRD spectra of this sample, Figure 9; showed the presence of secondary phases and byproducts when comparing to BFO samples (COD 1001090) (Gražulis, et al., 2012). The formation of these unwanted byproducts probably occurred during the calcination phases. In general, during the heating phase ($T = 200^{\circ}\text{C}$) the metal nitrates decompose to metal carboxylated and metal oxides while generating nitrogen oxides as toxic gases (Deng, Chen, & Tüysüz, 2016). Subsequently, in calcination phase at 500°C , the metal carboxylates start to decompose completely as metal oxides which in return start to react to the final product BiFeO_3 . Initially small particles of BiFeO_3 in the size range of the SBA-15 pore diameter, i.e. 8nm, start to form. These small nanoparticles then grow together over a time period of several hours and form the desired mesoporous precursor material (note: the material as this stage is not yet mesoporous as the template, i.e. SBA-15 has to be removed by NaOH leaching). However, while these high temperatures over a prolonged period are required for the material formation, bismuth volatilizes at this temperature, resulting in increased byproduct formation such as the iron rich phase $\text{Bi}_2\text{Fe}_4\text{O}_9$.

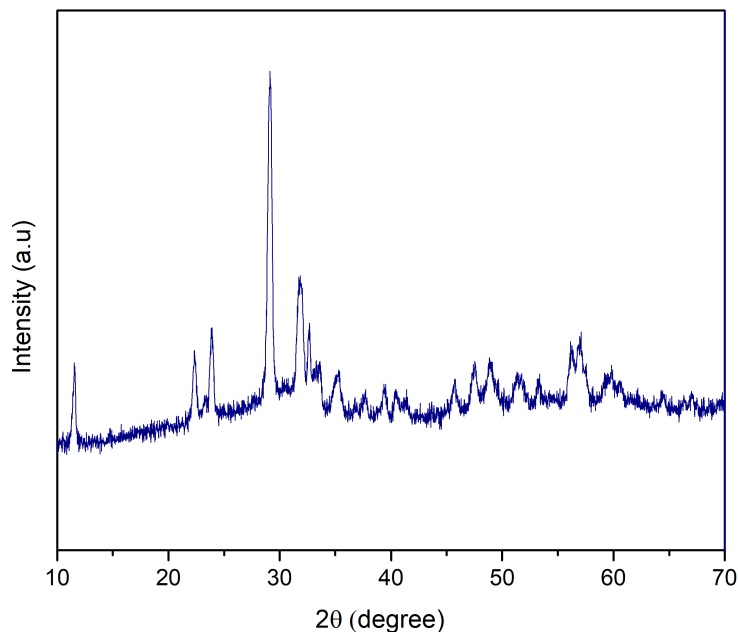


Figure 9: XRD patterns of BFO using oxalic acid in nanocasting technique.

3.1.2. Autocombustion Technique

X-ray powder diffraction (XRD) patterns of pure and Gd doped BFO samples obtained by the autocombustion method are shown in Figure 10. These diffraction results show the formation of pure BFO ($x = 0$) which crystallized in the rhombohedral lattice R3c (COD 1001090) (Gražulis, et al., 2012). For the Gd doped BFO samples, when increasing Gd concentrations a peak shift as well as the transformation of a splitted peak into a broad single at around 32 degrees peak can be observed (see Figure 10(b)). This feature suggests that a structural change can be observed due to the partial substitution of Bi^{3+} ions by Gd^{3+} . A similar behavior has also observed in Eu doped BFO materials (Liu, Fang, Zheng, Sheng, & Mingrong, 2009)

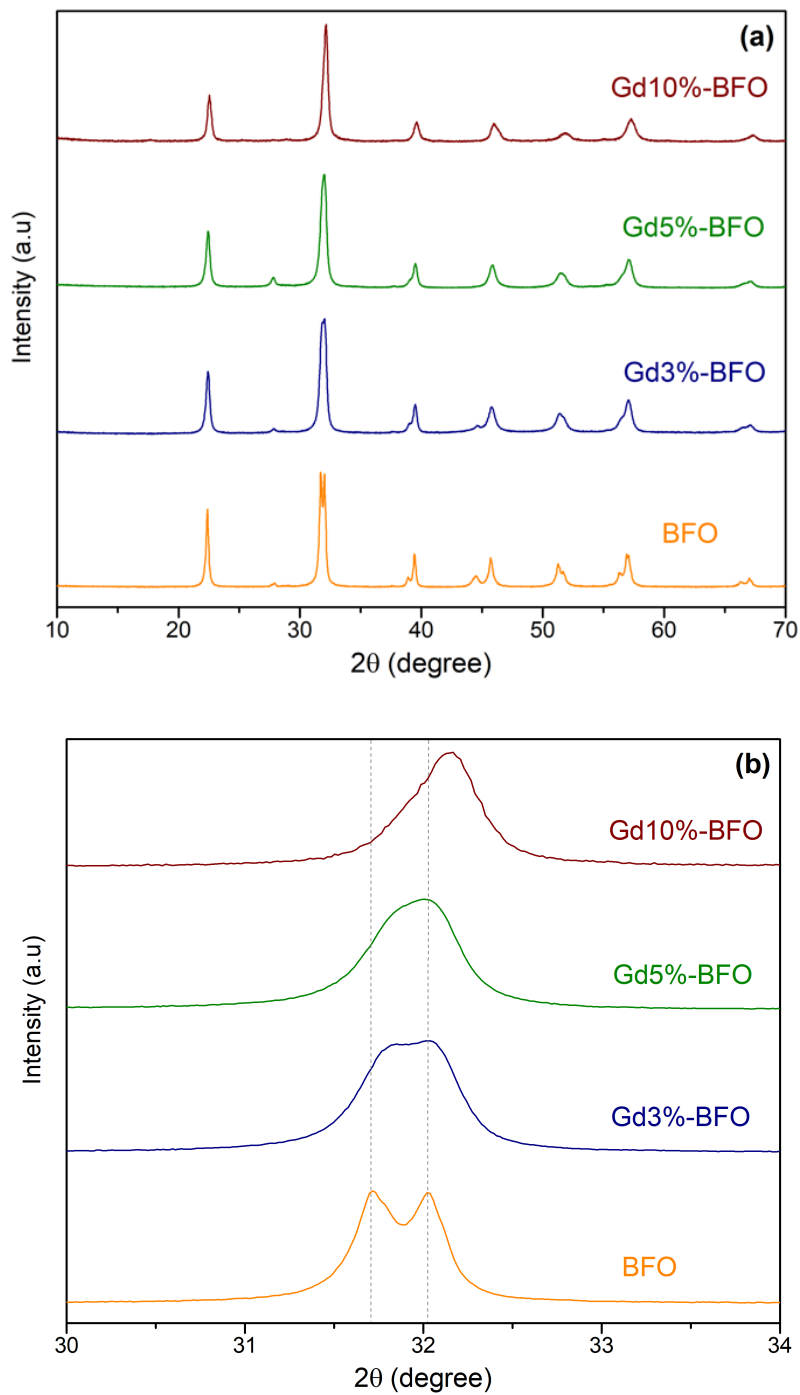
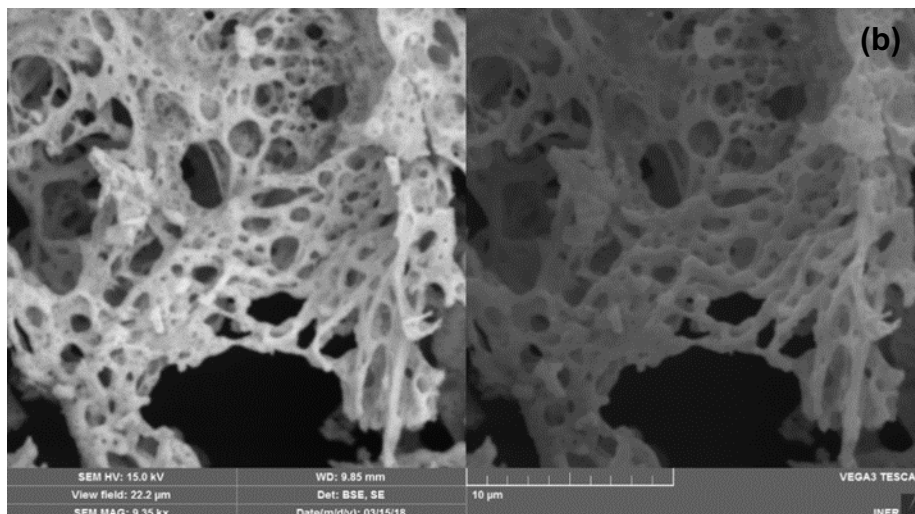
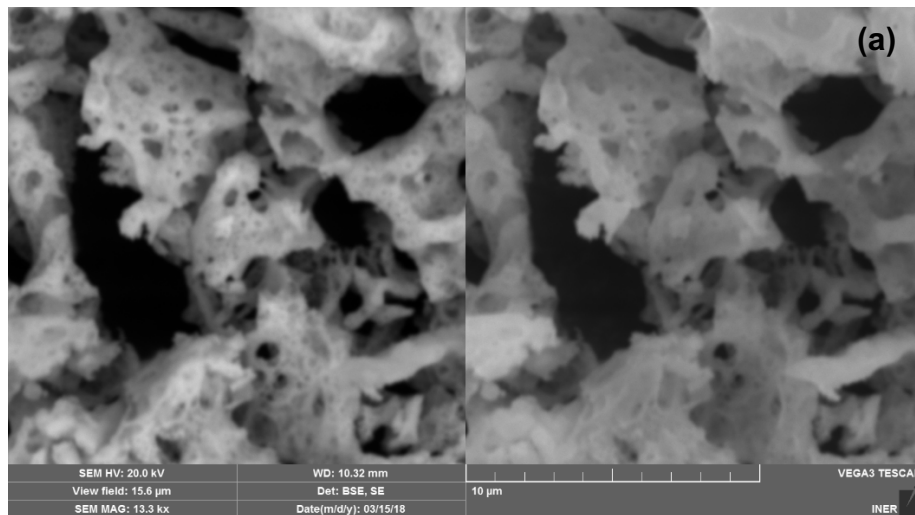


Figure 10 : (a) XRD patterns of $\text{Bi}_{1-x}\text{Gd}_x\text{FeO}_3$ ($x=0.00, 0.03, 0.05,$ and 0.10); (b) the zoom-in patterns of $\text{Bi}_{1-x}\text{Gd}_x\text{FeO}_3$ in the range of 30° to 34° .

The scanning electron microscopy (SEM) images of the pure BFO and Gd doped samples are presented in figure 11(a-d). Each image was collected using two different detector techniques. The left images correspond to back scattered electron and the right images are obtained by a secondary electron detector. As shown in figure 11, the obtained BFO materials are characterized by a highly porous network instead of agglomerated nanoparticles. The pores of pure BFO, Gd 3%, Gd 5% and Gd10% BFO exhibit irregular shapes and sizes ranging from nanometers to micrometers.



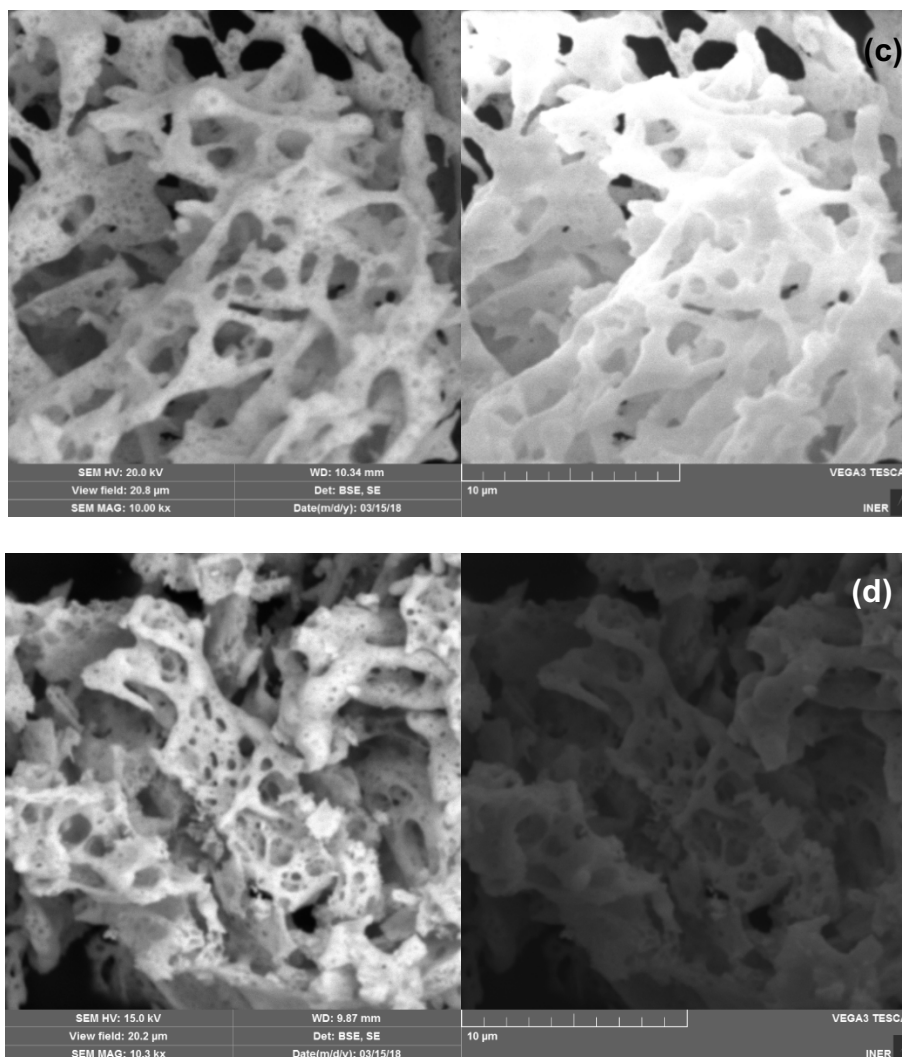


Figure 11: SEM images of synthesized samples: (a) pure BFO; (b) Gd 3%-BFO, (c) Gd 5%-BFO, (d) Gd 10%-BFO. The scale bar to all images is of 10 μm.

3.2. Band gap measurements

The optical properties of the doped and undoped BFO samples obtained by the autocombustion method were further investigated by UV-Vis diffuse reflection spectroscopy. As shown in Figure 12, the UV-Vis diffuse reflectance spectra of all samples were transformed by the Kubelka–Munk method (Kubelka & Munk, 1931). The absorption spectra show that all samples absorb a considerable amounts of visible light. This rather strong absorption lead to spectra with a very low signal to noise ratio. Thus, all spectra were smoothed using an adjacent averaging method with 25 points. The

energy band gap of the nanoparticles could then be calculated from the tangent line in the plot of the square root of Kubelka–Munk functions against photon energy.

The resulting energy band gaps decrease from 2.33 eV for the undoped BFO sample to 2.22 eV for all doped samples. It should be noted, that in the case of bismuth ferrite, band gaps correspond to particle sizes, i.e. a small band gap correlates usually with a small particle size. A band gap of 2.2-2.3 eV as obtained for the samples in this thesis, corresponds to a particle size in the nanometer regime. However, as the SEM images have shown clearly, the obtained samples are rather micrometer sized samples. This result can be explained by the influence of the porous nature of the samples which obviously affects the band gap properties. This leads to an interesting feature of these samples, i.e. even though the samples are micrometer sized they possess properties of nanometer sized particles.

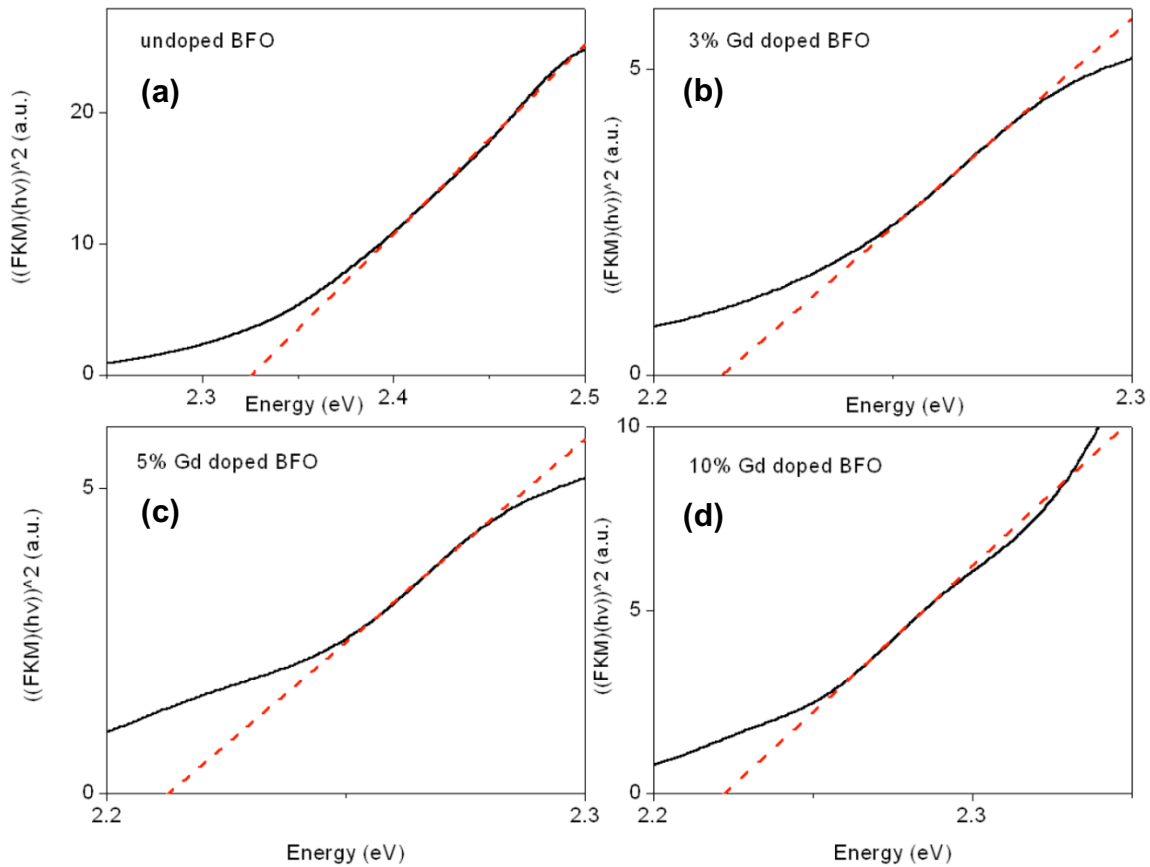


Figure 12: Band gaps plots: (a) pure BFO; (b) Gd 3%-BFO, (c) Gd 5%-BFO, (d) Gd 10%-BFO.

3.3. Photocatalytic Activity

The photocatalytic activity of the prepared samples were evaluated using the setup and conditions as described above. Figure 13 shows the photocatalytic degradation efficiency of Rhodamine B using pure BFO and Gd doped BFO photocatalysts as well as two control samples. After reaching an adsorption/desorption equilibrium state in the darkness, pure BFO, Gd 3%-BFO, Gd 5%-BFO, and Gd10%-BFO could adsorb approximately 14.35%, 14.55%, 6.90% and 11.52% of RhB molecules, respectively, during this initial dark phase. The adsorption tendency was not related to Yang, et al (2014) where more Gd content in BFO materials increased adsorption capacity; further studies are needed in order to evaluate Gd content and adsorption capacity of RhB.

Excluding the initial adsorption phase in darkness, the photodegradation of RhB after 240 min, was 14.35% (Gd3%-BFO), 34.03% (Gd5%-BFO) and 16.05% (Gd10%-BFO) whereas RhB degraded by 11.40 % using the undoped BFO sample. Furthermore, adding the degradation during the stirring period in darkness to the total degradation, pure BFO Gd3%-BFO, Gd5%-BFO and Gd10%-BFO decomposed RhB by 25.75%, 36.37%, 40.94% and 27.57%, respectively. As the degradation is highest using the Gd doped samples, these results show the positive effect of doping with Gd. The overall best catalyst is the doped Gd5%-BFO sample as it lead to the highest RhB degradation. Additionally, a blank control confirms no degradation of RhB occurs without the catalyst, while dark control also demonstrated that RhB does not degrade in the presence of a catalyst but in absence of light irradiation (after a small initial degradation). These test reactions confirmed, that indeed a photocatalytic degradation of the dye is occurring in which the prepared samples act as photocatalysts.

Similar results were presented by Zhang, et al., (2016). Undoped BFO catalysts which were synthesized by sol-gel method decomposed Rhodamine B by 22.3%. When Gd doped BFO samples were used in the photocatalysis, a significant increase was also noticed. After 270 min visible light irradiation time, Gd 3%-BFO and Gd5%-BFO degraded 56.8% and 42.1% respectively (Zhang, et al., 2016). In conclusion, compared

to pure BFO, the Gd doped BFO samples revealed enhance absorption capacity during visible irradiation phase.

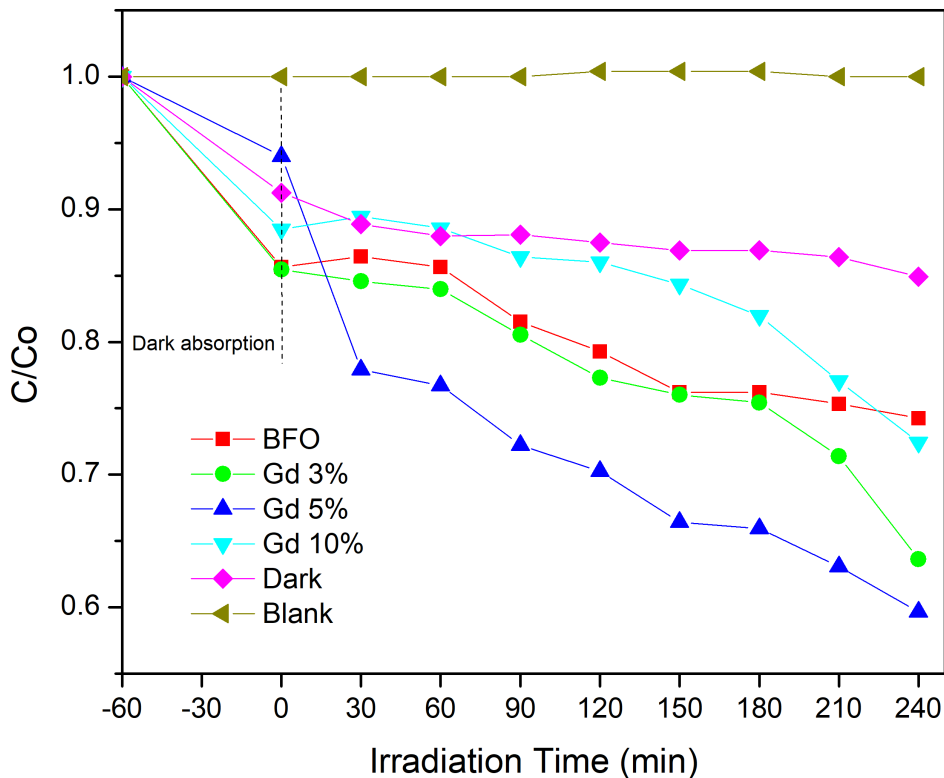


Figure 13: Photocatalytic degradation of RhB as a function of irradiation time (min) under visible light catalyzed by pure BFO, Gd doped BFO samples, dark and blank controls.

To quantify reaction kinetics of the RhB degradation, the experimental data shown in Figure 14 could be fitted by the Langmuir-Hinshelwood, equation (11), showing a pseudo first order kinetic reaction behavior. From the linear fitting curves, the RhB degradation rate constant k was calculated.

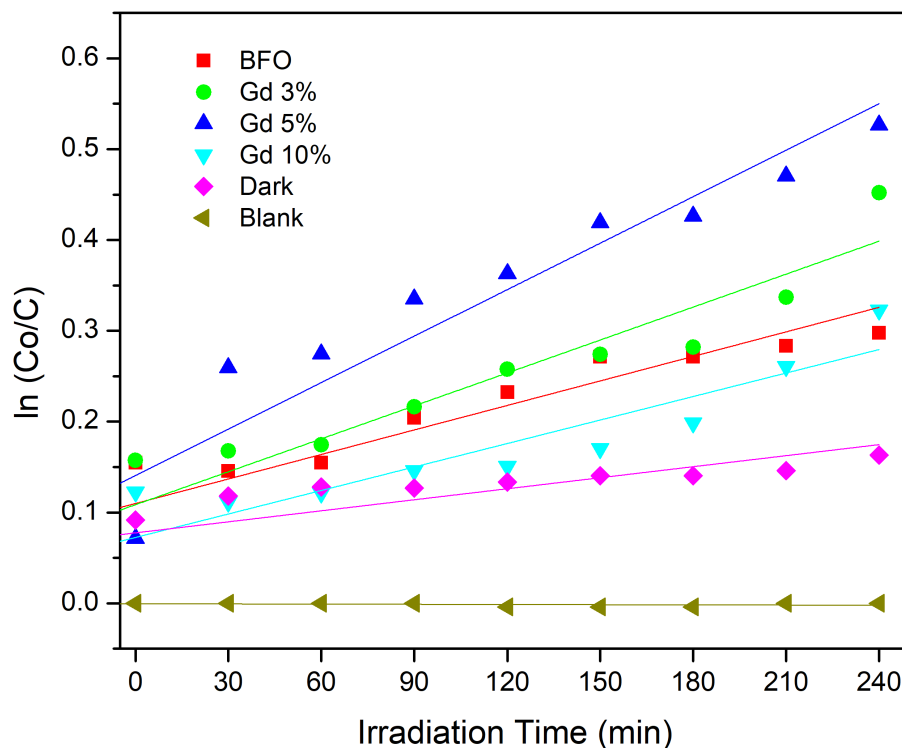


Figure 14: Pseudo- first order kinetics reaction fitting data for the photocatalytic degradation of RhB.

As presented in Table 4, the Gd5%-BFO exhibited the highest k value $1.58 \times 10^{-3} \text{ min}^{-1}$, which was 2.21 times that of pure BFO compound. Thus, the comparison of reaction rates shows again that an increase of Gd doping significantly enhances the photocatalytic degradation of RhB.

Table 4: Pseudo first order rate constants for RhB photodegradation and linear regression coefficients of each BFO samples

Photocatalyst	Rate Constant k (min^{-1})	Total Degradation (%)
BFO	7.14×10^{-4}	25.75
Gd3%-BFO	1.09×10^{-3}	36.37
Gd5%-BFO	1.58×10^{-3}	40.94

Gd10%-BFO	7.93×10^{-4}	27.57
-----------	-----------------------	-------

3.4. Optimizing Photocatalysis

3.4.1. Effect of Catalyst Concentration

One of the parameters which affects significantly the efficiency of photodegradation is the photocatalyst concentration (Al-Kahtani, 2017). To evaluate the effect, Gd5%-BFO was chosen due to the highest degradation rate and efficiency. Figure 15 compares the photodegradation efficiency of RhB employing 50 mg and 100 mg of photocatalyst per 50 ml of RhB solution at 5 mg/L. As expected, degradation efficiency increases with increasing photocatalyst concentration. While at an initial of 1 mg/mL the total degradation is 40.94%, an increase of the Gd5%-BFO concentration to 2mg/mL leads to a degradation of 65.29%. The reason of the degradation increment was related to the higher catalyst concentrations, which leads consequently to more active sites available for heterogeneous catalytic process. In other words, an increase of the catalyst contributed to an enhanced generation of hydroxyl radicals, which improved the photocatalytic degradation rate of RhB (Cui, et al., 2013).

3.4.2. Influence of Initial pH on photodegradation process

In literature, it is known that a decrease of pH (i.e. more acidic conditions) could lead to a protonation of the dye. Thus, the resulting dye in acidic conditions is likely to be a cation and thus a polar substrate. Since, the photocatalyst is also polar, attractive interactions between the catalyst and the dye are formed (Al-Kahtani, 2017) (Ling, Bhatia, & Zuhairi, 2010). A recent study of Merka show that at pH 4.7, attractive interactions between the protonated carboxyl group of the dye and the protonated catalyst surface are present (Merka, Yarovyj, Bahnemann, & Wark, 2010).

In our study, initially the RhB solution had a concentration of 5mg/L and a pH value of 6.70. In order to evaluate the influence of the pH in this particular photocatalytic process the reaction mixture was acidified to a final pH 4.0 by adding one small drop of nitric

acid to the solution. After that, all the process remained the same with 100 mg of photocatalyst. Figure 15 demonstrates a significant effect on RhB photodegradation, reaching a total degradation of 94.00% RhB.

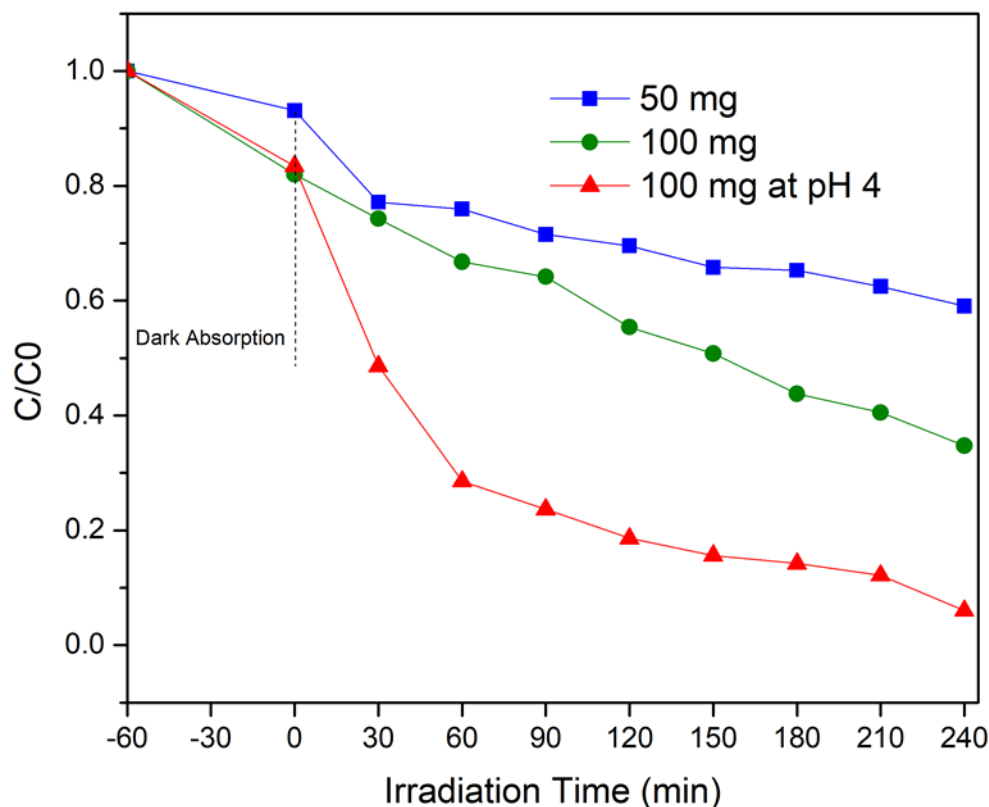


Figure 15: Catalyst Concentration and pH effect on photocatalytic efficiency using Gd5% doped BFO sample.

4. Conclusions

For the research, BFO were synthesized by two different techniques (nanocasting and autocombustion) to obtain a highly reactive catalyst i.e. porous material and be evaluated in photocatalytic activity for RhB degradation.

Nanocasting was based using a hard template in a wet impregnation-calcination method. Organic acids such as citric, oxalic and tartaric acid were added to evaluate their effect as chelating reagents. TEM images suggested a successful metal

precursor's impregnation in the channel of SBA-15. Unfortunately, byproducts and secondary phases were formed along BFO as shown in XRD diffraction patterns. The undesirable formation of these byproducts can be attributed to the high temperatures and calcination times during the last phase of the synthesis. In addition, reaction of the precursors, i.e. nitric acid, ethanol plus tartaric acid caused a dangerous exothermic reaction with nitrous oxides gases being violently released. In consequence, all samples using the nanocasting method were discarded and not used for photocatalytic evaluation.

Autocombustion technique demonstrated to be a facile technique resulting in the successful synthesis of BFO samples with a presumably high surface area due to porous nature. As shown in SEM images, irregular pore shapes and size ranges from nanometers to micrometers confirmed a highly porous network. Also, successful substitution of Bi by Gd was confirmed by XRD. When increasing Gd concentrations, a shift of a peak in the corresponding XRay diffractogram as well as the transformation of a splitted peak into a broad single was observed. Interestingly, the optical properties of the samples, i.e. the band gap, seem to be correlated to the porous nature of the samples. While the band gaps range from 2.22 eV to 2.32 eV nanometer sized samples were expected. However, SEM images clearly show micrometer sized samples. This can be explained by the direct influence of the porosity on the band gap.

For the photocatalytic activity, it was shown that the catalyst was responsible for dye degradation due to control tests. Moreover, compared to pure BFO, the Gd doped BFO samples revealed enhanced absorption as well as degradation capacity showing that Gd act as electron trapping spots to improve the production and separation of photogenerated electron-hole pairs. The optimum conditions for the highest Rhodamine B degradation (94.00%) was achieved for a 5 mg/L RhB solution at pH 4, a doped sample of Gd5%-BFO and a loading of 100 mg. At a lower pH, the dye is protonated and thus creating a polar substrate. Since, the photocatalyst is also polar, attractive interactions between the catalyst and the dye are formed, resulting an efficiency increment.

These results clearly reveal the importance of identifying the optimum technique for the photocatalyst synthesis, as well as optimum parameters for the degradation process in order to enhance the rate and degradation efficiency. Additionally, the investigation outcomes showed how undoped BFO and Gd doped BFO materials could degraded RhB concentration through time. Further studies are needed for an effective application in a major scale of photocatalytic oxidation processes. Also, BFO photocatalyst for photocatalytic oxidation processes is suggested to be a promising mechanism for dyes degradation from textile wastewater treatment due to high efficiency and simple implementation.

5. References

- Al-Kahtani, A. (2017). Photocatalytic Degradation of Rhodamine B Dye in Wasterwater Using Gelatin/ CuS/ PVA Nanocomposites under Solar Light Irradiation. *Journal Of Biomaterials and Nanobiotechnology*, 8, 66-82. doi:10.4236/jbnb.2017.81005
- Bai, X., Wei, J., Tian, B., Reiss, T., Guiblin, N., Gemeiner, P., . . . Canero, I. (2016). Size Effect on Optical and Photocatalytic Properties in BiFeO Nanoparticles. *The Journal of Physical Chemistry*. doi:0.1021/acs.jpcc.5b09945
- Cui, W., Ma, S., Liu, L., Hu, J., Liang, Y., & Gamage, J. (2013). Photocatalytic activity of Cd_{1-x}Zn_xS/K₂Ti₄O₉ for Rhodamine B degradation under visible light irradiation. *Applied Surface Science*, 271, 171-181. doi:10.1016/j.apsusc.2013.01.156
- Dao, N., Pham, N., Doan, T., Nguyen, T., Nguyen, Q., & Duong, T. (2016). Low-Temperature Synthesis and Investigations on Photocatalytic Activity of Nanoparticles BiFeO₃ for Methylene Blue and Methylene Orange Degradation and Some Toxic Organic Compounds. *Advances in Natural Science*, 7(4). doi:10.1088/2043-6262/7/4/045003
- Deng, X., Chen, K., & Tüysüz, H. (2016). A Protocol for the Nanocasting Method: Preparation of Ordered Mesoporous Metal Oxides. *Chemistry of Materials*. doi:10.1021/acs.chemmater.6b02645
- Dhananjai, B. (2016). *Explosion from Inappropriate Disposal of Nital in a Waste Nitric Acid Container*. Ontario: University of Waterloo.
- Gao, T., Chen, Z., Huang, Q., Niu, F., Huang, X., Qin, L., & Huang, Y. (2014). A Review: Preparation of Bismuth Ferrite Nanoparticles and Its Applications in Visible- Light Induced Photocatalyses. *Advanced Study Center*, 40, 97-109.
- Garcés, L., Mejía, E., & Santamaría, J. (2004). Photocalysis as an Alternative for Wastewater Treatment. *Lasallista*, 1(1), 83-92.
- Gražulis, S., Daškevič, A., Merkys, A., Chateigner, D., Lutterotti, L., Quirós, M., . . . LeBail, A. (2012). *Crystallography Open Database (COD): an open-access collection of crystal structures and platform for world-wide collaboration*. Nucleic Acids Research.

- Hashimoto, K., Irie, H., & Fujishima, A. (2005). TiO₂ Photocatalysis: A Historical Overview and Future Prospects. *Japanese Journal of Applied Physics*, 44(14), 8269-8285.
- Hwang, C., Sheng, J., & Huang, T. (2005). Combustion synthesis of Ni–Zn ferrite by using glycine and metal nitrated- investigations of precursors homogeneity, product reproducibility, and reaction mechanism. *Materials Chemistry and Physics*, 93(190), 330-336. doi:10.1016/j.matchemphys.2005.03.056
- IARC. (1998, 03 26). *Rhodamine B*. Retrieved from Inchem.org: <http://www.inchem.org/documents/iarc/vol16/rhodamineb.html>
- Kant, R. (2012). Textile Dyeing Industry and Environmental Hazard. *Natural Science*, 4(1), 22-26. doi:10.4236/ns.2012.41004
- Khataee, A., & Kasiri, M. (2010). Photocatalytic Degradation of Organic Dyes in the Presence of Nanostructured Titanium Dioxide: Influence of the Chemical Structure of Dyes. *Journal of Molecular Catalysis*, 328, 8-26. doi:10.1016/j.molcata.2010.05.023
- Kormann, C., Bahnemann, D., & Hoffman, M. (1988). Photocatalytic Production of H₂O₂ and Organic Peroxides in Aqueous Suspensions of TiO₂, ZnO and Desert Sand. *Environmental Science and Technology*, 22, 798-806. doi:10.1021/es00172a009
- Kubelka, P., & Munk, F. (1931). A contribution to the appearance of the Paint. *Journal of Technical Physics*, 12, 593-601.
- Kumar, B. (2009). *Synthesis of Multiferroic BiFeO₃ Material by Autocombustion Technique*. Thesis, National Institute of Technology, Department of Ceramic Engineering.
- Ling, Y., Bhatia, S., & Zuhairi, A. (2010). Process behavior of TiO₂ nanotube-enhanced sonocatalytic degradation of Rhodamine B in aqueous solution. *Separation and Purification Technology*, 77, 331-338. doi:10.1016/j.seppur.2010.12.023
- Liu, J., Fang, L., Zheng, F., Sheng, J., & Mingrong, S. (2009). Enhancement of Magnetization in Eu doped BiFeO₃ nanoparticles. *Applied Physics Letters*, 95(2). doi:10.1063/1.3183580

- Mamun, K., Kurny, A., & Gulshan, F. (2017). Parameters Affecting the Photocatalytic Degradation of Dyes Using TiO₂: A Review. *Appl Water Sci*, 7, 1569-1578. doi:10.1007/s13201-015-0367-y
- Merka, O., Yarovy, V., Bahnemann, D., & Wark, M. (2010). pH Control of the Photocatalytic Degradation Mechanism of Rhodamine B over Pb₃Nb₄O₁₃. *The Journal of Physical Chemistry*, 115, 8014-8023. doi:10.1021/jp108637r
- Nair, M., Kaliaguine, S., & Kleitz, F. (2014). Nanocast LaNiO₃ Perovskites as Precursors for the Preparation of Coke-Resistant Dry Reforming Catalysts. *American Chemical Society*, 3837-3846. doi:10.1021/cs500918c
- National Center for Biotechnology Information. (n.d.). Retrieved marzo 11, 2018, from PubChem Compound Database: <https://pubchem.ncbi.nlm.nih.gov/compound/6694>
- Nigam, P., Armour, G., Banat, I., Singh, D., & Marchant, R. (2000). Physical Removal of Textile Dyes and Solid State Fermentation of Dyes-adsorbed Agricultural Residues. *Bioresour*, 72, 219-226.
- Ortiz, J., Díaz, D., Zumeta, I., Arriola, H., Betancourt, I., Santiago, P., & Nava, N. (2013). Easy Synthesis of High Purity BiFeO₃ Nanoparticles: New Insights Derived from the Structural, Optical, and Magnetic Characterization. *Inorganic Chemistry*, 52, 10306-10317. doi:10.1021/ic400627c
- Papadas, I., Kota, S., Kanatzidis, M., & Armatas, G. (2012). Templated Assembly of BiFeO₃ Nanocrystals into 3D Mesoporous Networks for Catalytic Applications. *The Royal Society of Chemistry*. doi:10.1039/x0xx00000x
- Paredes, J. (2013). *Universidad de San Martín de Porres USMP*. Retrieved from <http://www.usmp.edu.pe/publicaciones/boletin/fia/info86/articulos/importanciaAgua.html>
- Pérez, G. (2015). Tratamiento de Aguas Residuales de la Industria Textil mediante Procesos Electroquímicos. Retrieved from <http://www.dspace.uce.edu.ec/bitstream/25000/4518/1/T-UCE-0017-116.pdf>
- Poots, V., & McKay, J. (1976). The Removal of Acid Dye from Effluent Using Natural Adsorbents. *Water Res*, 10, 1067-1070.

- Rinkesh. (2009). *40 Interesting Facts About Water Pollution*. Retrieved from <http://www.conserve-energy-future.com/various-water-pollution-facts.php>
- Robinson, T., McMullan, G., Marchant, R., & Nigam, P. (2001). Remediation of Dyes in Textile Effluent: A Critical Review on Current Treatment Technologies with a Proposed Alternative. *Biosource Technology*, *77*, 247-255. doi:10.1016/s0960-8524(00)00080-8
- Schneider, J., Matsuoka, M., Takeuchi, M., Zhang, J., Horiuchi, Y., Anpo, M., & Bahnemann, D. (2014). Understanding TiO₂ Photocatalysis: Mechanisms and Materials. *American Chemical Society*, *114*, 9919-9986. doi:10.1021/cr5001892
- Water Scarcity*. (2017). Retrieved from World Wild Life WWF: <https://www.worldwildlife.org/threats/water-scarcity>
- Willmott, N., Guthrie, J., & Nelson, G. (1998). The Biotechnology Approach to Colour Removal from Textile Effluent. *JSDC*, *114*, 38-41.
- Yang, Y., Zhang, T., Le, L., Ruan, X., Fang, P., Pan, C., . . . Wei, J. (2014). Quick and Facile Preparation of Visible light-Driven TiO₂ Photocatalyst with High Absorption and Photocatalytic Activity. *Scientific Reports*, *4*(7045). doi:10.1038/srep07045
- Zhang, N., Chen, D., Niu, F., Wang, S., Qin, L., & Huang, Y. (2016). Enhanced visible Light Photocatalytic Activity of Gd-doped BiFeO₃ Nanoparticles and Mechanism insight. *Nature*. doi:10.1038/srep26467

6. Annexes



Figure 16: Constructed photo reactor for photocatalytic degradation of RhB, by Thomas Cadenbach